Editors' Suggestion

Mitigation of the turbulence within an arteriovenous fistula with a stent implantation

Sanjiv Gunasekera [1,*] Tracie Barber [1] Olivia Ng [1] Shannon Thomas,[2] Ramon Varcoe [2] and Charitha de Silva[1]

[1]*School of Mechanical of Manufacturing Engineering, The University of New South Wales, 2052, NSW, Australia*

[2]*Department of Vascular Surgery, Prince of Wales Hospital, Randwick, 2031, NSW, Australia*

(Received 1 August 2022; accepted 14 November 2022; published 8 December 2022)

The transitional flow which initiates within the junction (anastomosis) of an arteriovenous fistula (AVF) is known to be a contributing factor in the onset of vascular disease. A novel treatment method involving the implantation of a flexible stent across the anastomosis has enabled the retention of a large proportion of functioning AVFs, despite the propensity for stent malapposition to occur at the sharp inner curve of the anastomosis. Large eddy simulations of a single patient-specific AVF with and without the presence of a stent captured oscillatory flow behavior emanating from the interface of the two inlet flows in the stent-absent case, however, these oscillatory features were subdued in the stented case. The stent-absent case generally had higher turbulent kinetic energy (TKE) in the anastomosis which led to larger cycle-to-cycle variations in wall shear stress (WSS). The significantly lower TKE generated at the heel of the stented AVF was contained within the malapposed stent, thereby resulting in lower WSS fluctuations. However, a slight increase in turbulence downstream of the malapposed stent edge was noted. This detailed study reveals a significant decrease in turbulence within the AVF in the presence of the stent, thereby providing a level of understanding underpinning the success of the treatment strategy (in this patient case) from a fluid dynamic perspective.

DOI: 10.1103/PhysRevFluids.7.123101

I. INTRODUCTION

Chronic kidney disease is the progressive decrease of kidney filtration ability with the last stage of this condition known as end stage renal disease (ESRD). At this stage, the majority of patients that are not granted kidney transplants opt for hemodialysis where the blood is filtered outside the body in a dialysing machine. This option requires vascular access which is usually achieved by creating an arteriovenous fistula (AVF) [1], which is a surgical connection created between an artery and vein in the forearm. In addition to surgical trauma and a uremic environment, hemodynamic stress is a key factor attributed to the onset of vascular disease which leads to the failure of an AVF [2]. The initiation of transitional flow behavior at the anastomosis (junction) of the vasculature has been observed in CFD simulations [3–5] and a tomographic particle image velocimetry (Tomo-PIV) measurement [6] of AVF models noting the gradual dissipation of the turbulent energy as the flow traverses downstream along the vein. Turbulent flow behavior has also been noted in pulsatile direct numerical simulations of a flow within a stenosed (disease manifested as a vessel constriction) blood vessel at Reynolds numbers similar to those within an AVF [7]. A characteristic feature of the flow within an AVF is the stagnant recirculating low velocity flow downstream of the anastomosis [6]

*sanjiv.gunasekera@rmit.edu.au

leading to varying wall shear stress (WSS) that has been postulated to be an initiator of vascular disease [8].

Stents, which are metallic mesh-like scaffolding devices that hold open narrowing diseased vessels, have been used sparingly in AVFs due to the concerns associated with hindering cannulation [9] and unintended migration of the stent [10]. However, recent use of nitinol stents, known for their elasticity thereby increasing the shape conformity to tortuous vessels [11], have yielded high unassisted patencies [12–14] retaining a large proportion of functioning AVFs.

A side-effect of implanting the flexible stent across the sharp-angled anastomosis is the malapposition of the stent (sometimes referred to as the incomplete stent apposition), where the device is not completely embedded against the wall of the vessel. An undersized stent implantation is known to be a predictor of stent thrombogenicity [15] and the malapposition of the stent has been shown to produce recirculation regions near stent struts, along with the increase in areas of low time-averaged wall shear stress (TAWSS) [16,17]. However, with the increase in the degree of undersizing beyond 5% of the vessel diameter (equivalent to a decrease in stent lumen area below 90.25% of the vessel lumen) a decrease in the heterogeneity of the WSS was evident across the vessel [18]. Flow simulations of patient-specific models have also observed a lower coverage of adverse TAWSS in the presence of a malapposed stent [19]. A recent study has shown that undersized stent-grafts used to treat cephalic arch stenoses associated with AVFs have yielded higher access patency rates and a decrease in interventions [20].

Comparison of the AVF flow field with and without the flexible stent implantation highlighted the significant funnelling of flow within the malapposed stent encapsulated region, potentially containing the adverse hemodynamic behavior away from the vessel wall [21]. This funnelling characteristic is commonly leveraged in intracranial vasculature to divert flow away from aneurysms [22]. Additionally, the flow downstream of the anastomosis in the stented AVF reattached in a shorter space resulting in a smaller recirculation zone, thereby decreasing the adverse WSS behavior [21].

The present study aims to characterize the turbulent behavior of AVF flow in the presence of the stent, unravelling the interaction between the bulk flow funnelling feature of the stent and the inherently turbulent AVF anastomosis. To this end, the turbulent flow features are resolved with large eddy simulations (LES) of a single patient-specific AVF with and without the presence of a stent implantation. The same vessel geometry is used to isolate the influence of the stent. Comparisons of the fluctuating bulk flow field are followed by the assessment of the cycle-to-cycle variations in WSS.

II. METHODOLOGY

A. Patient data retrieval

The AVF of a 78-year-old male volunteer (at rest) was scanned with informed consent under the approval of the low/negligible risk (LNR) application with the South Eastern Sydney Local Health District Human Research Ethics Committee number 15/063 (LNR/16/POWH/7). A noninvasive three-dimensional freehand ultrasound scanning method was used to obtain the geometry of the AVF [23]. The ultrasound images were synchronized with the location of the ultrasound probe using an in-house code, to create a volume of scans. Subsequently, manual segmentation along with 3D Gaussian smoothing functions, conducted in Simpleware ScanIP image processing software (Synopsys Inc., CA), resulted in the reproduction of a surface mesh file (in the STL format) of the vessel lumen. Iterative adjustments to the manual segmentation were made by comparing the surface mesh of the vessel with the volume of scans, thereby minimizing the error due to the manual procedure.

The initial ultrasound scans could not be used to segment the stent due to the presence of excessive artefacts and the inherent low resolution of the scanning methodology. To capture relatively higher resolution images of the stent using a micro-CT scanner a polydimethylsiloxane (PDMS)

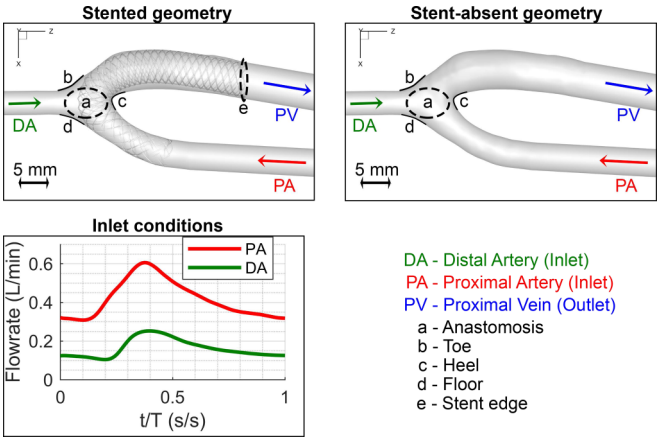

FIG. 1. Geometry and boundary conditions of the AVF models. The stented (top left) and stent-absent (top right) AVF geometries have been annotated with key regions of the vasculature. The inlet flow rate profiles applied at the proximal artery and distal artery are displayed at the bottom left.

phantom of the AVF geometry was fabricated [24]. PDMS was cast around a water-soluble 3D print of the AVF geometry which was eventually flushed out. A 5 mm diameter Supera stent (Abbott Vascular, Santa Clara, CA) was deployed (by a vascular surgeon) into the PDMS model. Stent malapposition, similar to observations in clinical circumstances [13], was noted at the heel of the anastomosis. To obtain a precise rendering of the stented AVF model, a micro-CT scanner (MILabs U-CT at MWAC, UNSW Sydney) with a step angle of 0.25°, was used to obtain an ultra-focus scan at an approximate overall resolution of 40 μm. The resulting high-resolution scan volume was segmented to generate an STL of the stent geometry and the segmentation of the vessel geometry was repeated to locate the AVF vessels in the same local coordinate system of the stent STL as shown in Fig. 1.

The stent and vessel geometries were smoothed using several iterations of a Gaussian smoothing algorithm. To ensure the stent strut diameter was equivalent to 152 μm (the physical stent strut diameter), sections of the segmented stent radius were measured by calculating the distance between the stent strut centerline and the closest STL surface elements. This method was used after each smoothing iteration to ensure an appropriate level of surface smoothness was achieved whilst avoiding overly shrinking the stent STL.

The spectral doppler function of the ultrasound machine was used to extract the patient-specific flow rate boundary conditions of the inlet vessels [25]. The patient AVF under consideration had a retrograde inlet flow configuration where the proximal artery and the distal artery supplied blood to the outlet vein of the AVF. Since the inlets of the two vessels were recorded individually, a simultaneous ECG trace was recorded using a three-lead ECG. The peak of the "QRS" complex of the ECG trace was used to temporally synchronize the inlet waveforms of the two vessels. The digitizing procedure, detailed in Carroll *et al.* [25], ensured that the commonly encountered noise accompanying the Doppler signal was minimized by cycle-averaging, median filtering, and Gaussian smoothing.

B. Numerical calculation setup

The presence of flow transitioning from the laminar regime, particularly in the deceleration phase of pulsatile flow, within vascular geometries has been noted in direct numerical simulations (DNS) [7,26]. Therefore, to understand any hemodynamic disturbances within the AVF, a simulation that is able to resolve any turbulence generation is of value. Since obtaining the spatial and temporal resolution to conduct a DNS is highly resource intensive, an LES that resolves a significant

portion of the turbulence generation can provide inferences of the behavior of larger, higher energy containing eddy disturbances while modeling the energy of the eddies smaller than the grid size. To resolve larger scales while modeling smaller scales, an LES makes use of a spatial filter which results in the filtered Navier-Stokes equations as follows:

$$\nabla \cdot \tilde{U} = 0, \tag{1}$$

$$\rho\left[\frac{d\tilde{U}}{dt} + (\tilde{U} \cdot \nabla)\tilde{U}\right] = -\nabla\tilde{P} + \mu\nabla^2\tilde{U} - \nabla \cdot \tau_{\text{SGS}}. \tag{2}$$

The filtered velocity and pressure variables are denoted by $\tilde{U}$ and $\tilde{P}$, respectively. To close the filtered Navier-Stokes equations, values for the subgrid scale turbulent stresses, denoted by τ_{SGS}, are modeled. The dynamic Smagorinsky subgrid scale (SGS) model was chosen to capture the lower energy disturbances and contribute to the dissipation of turbulent energy. The dynamically varying Smagorinsky constant (C_S) together with the mixing length estimates the subgrid energy in wall bounded flow [27,28]. Although this SGS is known to be overly dissipative at regions of separating flow [29,30], studies of stenotic flow have shown that the model replicates the mean flow and turbulent statistics well when compared with results from DNS [31–33]. Similarly, a patient-specific study of a stenosed region in a carotid artery demonstrated that LES with the dynamic Smagorinsky model was able to replicate the mean flow and turbulent features with pulsatile inlet conditions [34], thereby showing the applicability of the SGS model in the current AVF study as well.

The fluid domain was initialized using a Reynolds-averaged Navier-Stokes (RANS) simulation with the $k - \omega$ shear stress transport turbulence model as detailed in previous studies [21,24,25,35]. The fluid region of the AVF geometry was discretized by creating a tetrahedral mesh in the bulk flow and boundary layer regions using ICEM CFD (ANSYS Inc.). The grid convergence index (GCI) [36] was calculated by using the average of the velocity magnitude across a vessel lumen slice in the vein. The average GCI values were 0.016% and 1.95% for the stented and stent-absent geometries, respectively. Additionally, circumferentially averaged wall shear stress (WSS) values along the vein were compared against those from the coarse and fine mesh. The WSS values were largely seen to match the values of the fine mesh in both geometries with an average relative error of 1.86% and 1.63% for the stented and stent-absent geometries, respectively. Therefore a sufficient level of spatial discretization was achieved with 19.75 million elements for the stented geometry and 4.89 million elements for the stent-absent geometry to conduct the initial RANS simulations. With the progression to the LES, the mesh was further refined in specific locations in the domain by applying a mesh adaption algorithm at four time points. The algorithm refined elements, with a value of the gradient of subgrid dynamic viscosity, greater than a stipulated value. Application of this targeted mesh refinement methodology resulted in meshes composed of 24.60 million and 6.91 million elements for the stented and stent-absent cases. The average cell edge length on the stent wall was 32.5 μm which resulted in approximately 17 cells back-to-back across the circumference of a 152 μm stent strut. The average cell edge length on the vessel wall was 103 μm which resulted in approximately 176 cells back-to-back across the circumference of a vessel segment that is 5 mm in diameter. Using the stent strut diameter and the average outlet velocity (as the malapposed stent struts faced high velocities), flow with a Reynolds number of 25 would be the maximum faced at the stent struts. The detail of the mesh at the stent wall and vessel wall have been illustrated in Fig. 2.

It is recommended that an LES is capable of resolving 80% of the turbulent kinetic energy (TKE) [37]. This requirement was assessed, to determine the appropriateness of the level of spatial resolution, by comparing the resolved TKE against the total TKE (inclusive of that within the subgrid) as detailed in the Appendix. The average proportion of $\text{TKE}_{\text{resolved}}$ across the domain, calculated at the maximum inlet flow time point, was 96.8% and 97.03% for the stented and stent-absent models, respectively, thereby showing that the spatial resolution of the mesh was largely sufficient. The average $y+$ from the vessel wall across the domain at the maximum time point was

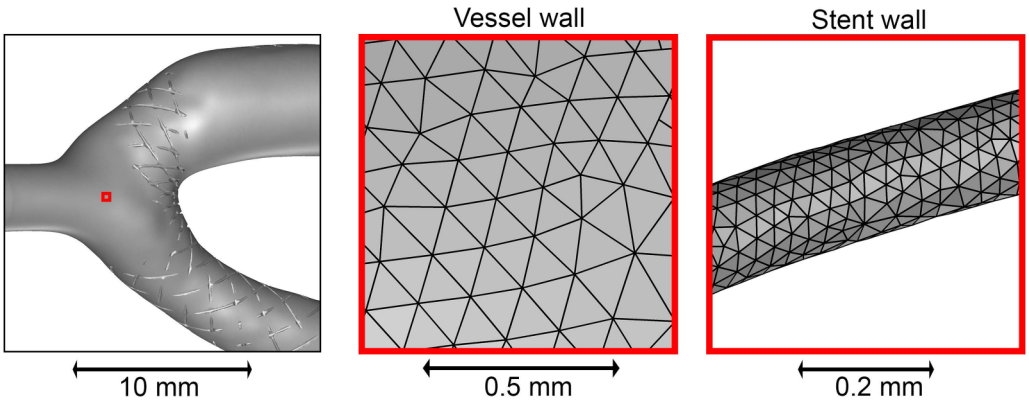

FIG. 2. Detailed view of cells at the vessel and stent wall boundaries near the anastomosis as annotated by the red box in the left subfigure. The average cell edge length on the vessel wall (middle) was 103 μm and the average cell edge length on the stent wall was 32.5 μm.

0.51 and 0.45 for the stented and stent-absent cases. Therefore, the majority of the near-wall cells were placed well within the viscous sublayer, thereby accurately calculating the wall shear stresses.

The pulsatile patient-specific inlet flow waveforms were applied at the proximal artery and the distal artery boundaries of the AVF geometry. The recorded heart rate of the patient was 60 bpm which was matched in the simulations by setting the period of the inlet waveforms to 1 s. The proximal vein was maintained as a nontractive outlet condition with relative pressure held at zero. To ensure the inlet flow waveforms had a developed flow profile, the ends of the vessels were extended by 10 times the diameters of the relevant vessel. The initial transient RANS was conducted with a fixed time-step of 0.001 s. Comparison of the slice-averaged velocity magnitude values between a time-step of 0.001 s and 0.0001 s showed a difference of 0.0218% and 0.166% for the stented and stent-absent cases, respectively. The difference in the circumferentially averaged WSS measurements were 1.50% and 1.52%, respectively, therefore the time-step of 0.001 s was deemed suitable. With the increased resolution of the spatial discretization for the LES, the temporal discretization required refinement as well to maintain the Courant-Friedrich-Lewy (CFL) below 1, such that the distance traveled by the flow within a time-step, remains within the bounds of the cell [38]. After decreasing the time-step to 0.0002 s, the average Courant numbers across the domain at the maximum inlet time points were 0.45 and 0.51 for the stented and stent-absent models, respectively.

The vessel and stent walls were set up with a no-slip wall condition and without compliance. A comparison between a stationary wall to a compliant wall in AVF flow simulations has shown that the resulting WSS trends remain similar with a general overestimation of the values at regions of low WSS in the case of the stationary wall [39]. The fluid properties were set to replicate the average blood physical properties with a density of 1060 kg/m^3. The effect of the non-Newtonian nature of blood, known to be minimal at the high shear rates [40] encountered in an AVF, was modeled using the Carreau model [41].

The pressure and velocity variables were solved using the pressure-based SIMPLE algorithm. A second-order upwind scheme was used for the spatial discretization of pressure quantities and a bounded central difference scheme was used for the spatial discretization of momentum quantities. A second-order implicit scheme was used for temporal discretization. Comparison of the resulting phase-averaged velocity magnitude flow field at the maximum time point with an equivalent flow field within the stent-absent AVF geometry obtained from a Tomo-PIV measurement [6] revealed consistent behavior as detailed in Sec. III. The average difference between the values from both measurements across three rakes in the vein was 0.13 m/s.

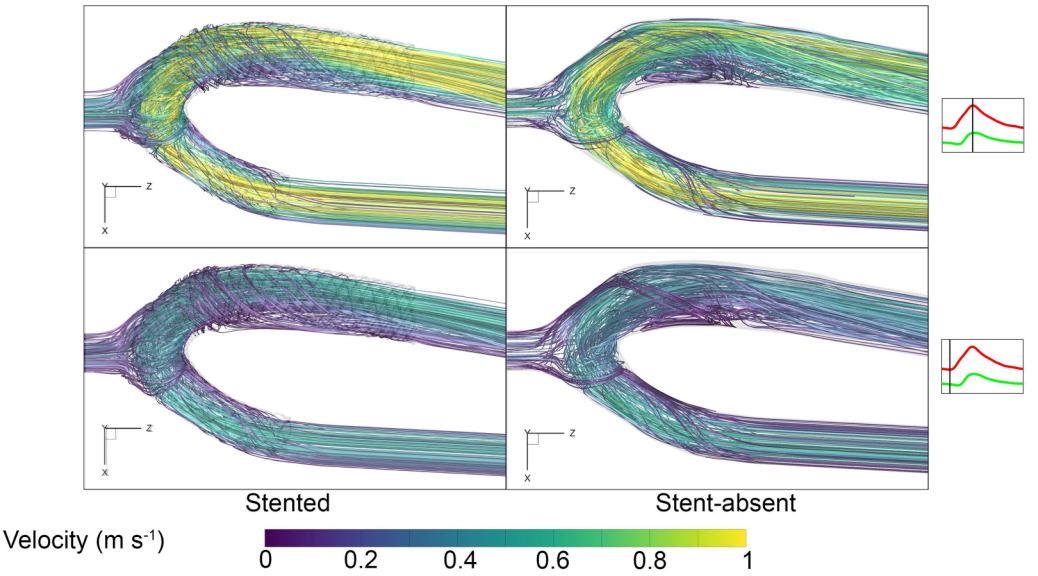

FIG. 3. Streamlines colored with the phase-averaged velocity magnitude at the maximum (top) and minimum (bottom) time points. The streamlines are illustrated for both stented (left) and stent-absent (right) cases.

The resulting bulk flow field behavior has been analyzed and compared in Sec. III while the WSS behavior has been investigated in Sec. IV. To visualize various WSS metrics throughout the circumference of the vessel wall, a surface unravelling procedure (detailed in Sec. IV) was followed resulting in the conversion of the tortuous vein and distal artery walls into 2D surfaces.

III. INFLUENCE OF STENT ON VENOUS BULK FLOW BEHAVIOR

A. Bulk flow oscillations

As noted in previous studies, the flow within the AVF geometry is highly three-dimensional in nature as seen in the illustration of the streamlines colored with the phase-averaged velocity magnitude values at the maximum and minimum time point (Fig. 3). High-velocity flow travels from the proximal artery and towards the vein in the central region of the vessel in both geometries. The flow from the distal artery manoeuvres around this central region of high velocity, eventually reattaching in the vein. The recirculation region captured at the heel of the anastomosis in the Tomo-PIV measurement of the stent-absent geometry [6] was noted in Fig. 3 as well. The spatial extent of the recirculation varied at both times thereby contributing to varying WSS behavior at that location. The streamlines in the stented geometry realigned to the flow normal direction much earlier resulting in an insignificant recirculation region.

To further detail the flow behavior noted in the vein of the AVF, in the current study, five monitor points were placed along the center of the vein starting from the anastomosis within both the stented and stent-absent geometries as shown in Fig. 4. The velocity magnitude signal recorded at these points was decomposed using Welch's power spectral density (PSD) estimator with a window length equal to the period of a cycle resulting in 12 segments. The segments were windowed using a Hanning window with an overlap of 50%. The sampling frequency was 50 kHz, thereby using every time-step. The 12 computed periodograms were then averaged to obtain the persisting spectral behavior. As expected, the global maximum amplitude for all signals took place at the patient's heart rate with a decrease in amplitude with the increase in frequency. However, clear local amplitudes were noted at 20 Hz and between 50 Hz and 70 Hz in the stent-absent AVF. This behavior was predominantly occurring at the first three monitor points (the first row of Fig. 4) which were located

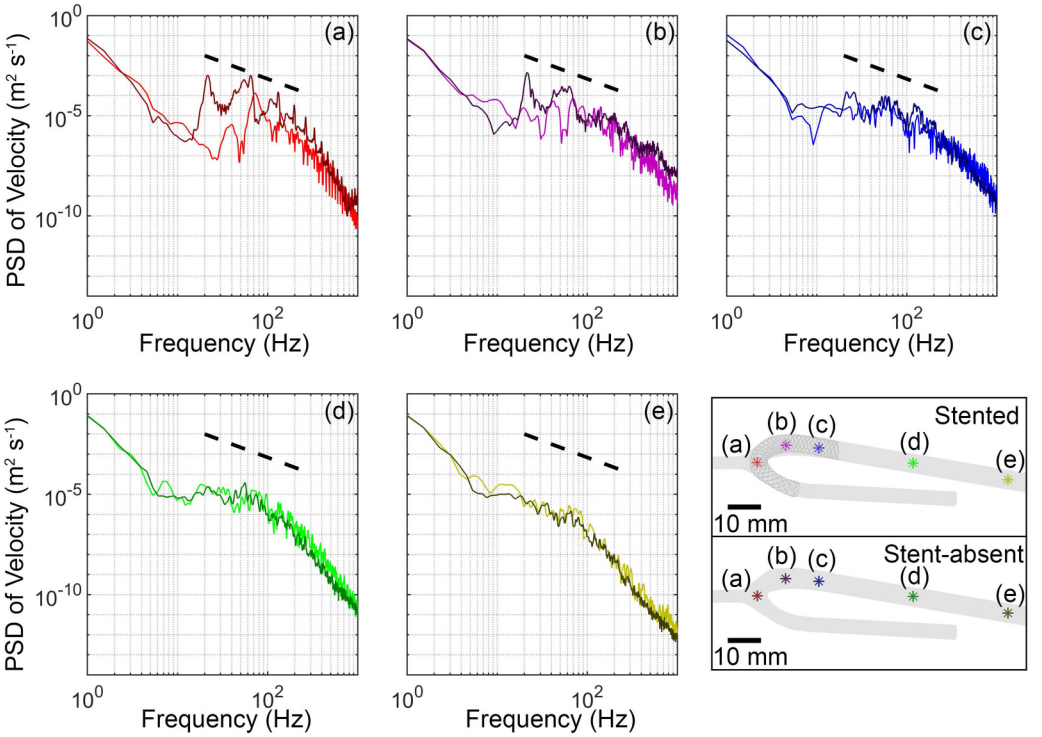

FIG. 4. Spectral decomposition of the velocity magnitude time-traces at monitor points along the vein for the stented and stent-absent cases. The darker lines correspond to the stent-absent case while the lighter lines correspond to the stented case. The dotted black line indicates the '-5/3' slope. The monitor point locations (0 mm, 11 mm, 21 mm, 50 mm, and 79 mm away from the anastomosis along the centerline) shown in the subfigure at the bottom right, link to the spectral plots by color.

at or close to the anastomosis. There were local peaks noted in the signals of these monitor point locations from the stented AVF as well, although the amplitudes of these peaks were much lower. The oscillatory flow behavior in the stented geometry was noted to occur between 70 Hz and 80 Hz. These oscillatory flow events settled as the flow traveled further downstream of the vein in both geometries (as illustrated in the second row of Fig. 4). The energy generated from these peaks (in both geometries) decayed with a slope close to a logarithmic gradient similar to that of turbulent decay (in the inertial subrange) as illustrated in Fig. 4. The decay at the monitor points further downstream from the anastomosis also followed a similar slope but at a much lower amplitude.

These findings suggest that there are significant oscillatory flow features initiating in the anastomosis and persisting through the juxta-anastomotic venous segment in the absence of the stent. Instantaneous velocity magnitude contour plots on the central plane of the anastomosis, shown in Fig. 5, provide further detail on the aforementioned oscillatory behavior. The instantaneous flow fields were separated by 0.009 s thereby aiming to capture the peaks and troughs of flow oscillations that were occurring at frequencies around 55.56 Hz. There is a significant change in the spatial location of the high velocity magnitude region at the upper wall of the vein in the stent-absent case. This behavior can be traced back to the anastomosis where the two opposing inlet flows interact with each other. The location of the low velocity magnitude region at the floor of the anastomosis moved a distance of approximately 1.6 mm back and forth due to the interaction of the inlet flows. Similar behavior was noted in the Tomo-PIV measurements with the low velocity magnitude region at the anastomosis floor moving a distance of 1.3 mm. In the stented case this interaction takes

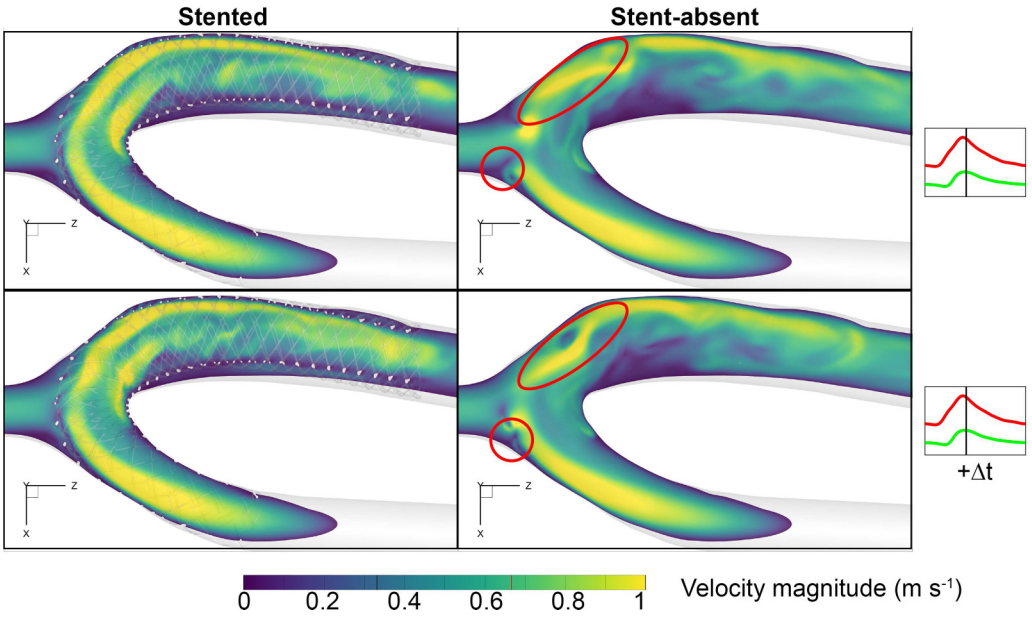

FIG. 5. Contour plots of instantaneous velocity magnitude on the central plane of the anastomosis. The distribution is illustrated near the maximum time point with a time separation $\Delta t = 0.009$ s. Annotations in the stent-absent geometry highlight the oscillations of the flow initiating from the interface of the two inlets.

place closer to the toe of the anastomosis, however, the strength of this behavior is much less significant with the oscillations drowning out as the flow traverse across the vein. Furthermore, the oscillations occurring in the stent-absent AVF persist throughout the cardiac cycle, however, the oscillations in the stented AVF occur only during the deceleration phase of the cardiac cycle (as seen in the Supplemental Material video [42]). One reason for the more subdued nature of the inlet flow interaction in the stented AVF is that the distal artery flow is distributed more evenly across the vessel cross-section with the presence of the porous stent however, in the stent-absent AVF, a larger peak is created due to the velocity profile spread across a larger cross-section thereby creating a larger contest with the higher flow coming from the proximal artery.

Another flow behavior that varies in this short time separation is the low velocity magnitude region at the heel of the stent-absent AVF. The flow that navigates the curved trajectory across the anastomosis eventually separates leading to oscillatory flow behavior. As before, this behavior is less pronounced in the stented AVF possibly due to the rough wall surface caused by the texture of the stent surface resulting in a delayed separation.

B. Turbulence generation within the AVF

To quantify the fluctuations generated in the LES of the two AVF cases, TKE was calculated using Eq. (3):

$$\mathrm{TKE} = \tfrac{1}{2}\left(u'^2_x + u'^2_y + u'^2_z\right). \tag{3}$$

Here, $u'_x = U_x - \overline{U_x}$, $u'_y = U_y - \overline{U_y}$, and $u'_z = U_z - \overline{U_z}$ correspond to the instantaneous velocity fluctuations, where $\overline{U_x}$, $\overline{U_y}$, and $\overline{U_z}$ are the phase-averaged velocities. The TKE was phase-averaged over 12 cycles to ensure that the quantity was converged. The distribution of the TKE across a central plane cutting through all vessels at the anastomosis is illustrated in Fig. 6. The general level of turbulence generation is much lower (by approximately an order of magnitude) in the stented case when compared to the stent-absent case.

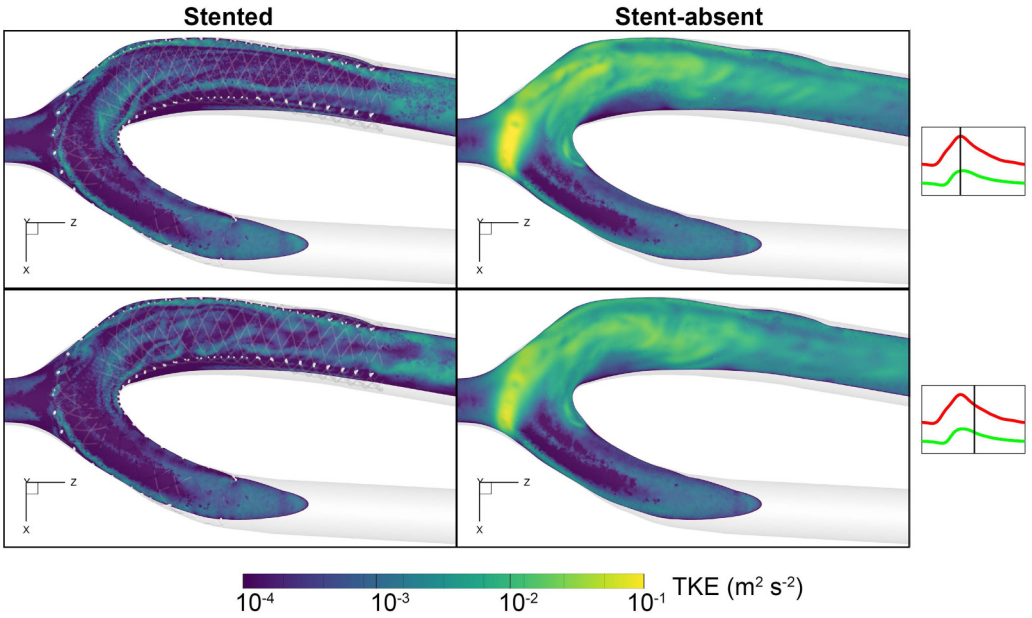

FIG. 6. Contour plots of turbulent kinetic energy (TKE) on the central plane of the anastomosis. The distribution of the TKE is illustrated at the maximum (top) and deceleration (bottom) inlet flow time points for both stented (left) and stent-absent (right) cases.

High TKE persisted throughout the cardiac cycle at the distal region of the anastomosis in the stent-absent case. This region coincides with the oscillations in velocity magnitude noted in the stent-absent case. The variations in velocity from cycle-to-cycle, when there is a slight phase difference in the oscillations, contribute to this increase in turbulence. In contrast to the stent-absent case, the TKE generation at the distal region of the anastomosis in the stented case is almost two orders of magnitude lower. The TKE magnitude at the interface of the two inlets is equivalent to the magnitude noted at the walls of the proximal artery and distal artery. Fluctuations larger than those expected in the near-wall regions are absent or insignificant in the stented case (at the interface of the two inlet flows).

The magnitude of the oscillatory behavior at the interface of the two inlet flows in the stented case was low, as noted by the spectral decomposition at the first monitor point in Fig. 4 and the instantaneous velocity plots of Fig. 5. Therefore, cycle-to-cycle variations of this behavior contributed to lower fluctuations in the stented case. An LES study of flow across the junction of a mixing tee noted the significant reduction in temperature fluctuations with the presence of a porous interface [43]. The averaged flow fields of the case with the porous junction also showed smoother velocity vectors towards the outlet. Similar dynamics could be at play with the presence of the stent (acting as the porous interface) obstructing the incoming distal flow (that could be likened to the branch of the mixing tee) yielding a smoother outlet flow with lower fluctuations.

In addition to this source of turbulence generation, the heel region of the stent-absent anastomosis was another location where high TKE flow was emanating. The spatial extent and the magnitude of the TKE increased at the maximum inlet flow time point and was sustained in the deceleration phase of the inlet flow. Regions of high standard deviation of velocity have been noted at the anastomosis with a further increase at the heel during the deceleration phase (particularly with the intermediate angle) in a parametric study of AVF geometries with varying anastomosis angles [5]. Similar increases in disturbances at the anastomosis have been noted in other studies of AVF geometries [4,44] where it was postulated that the spiralling flow separated at the heel. Flow

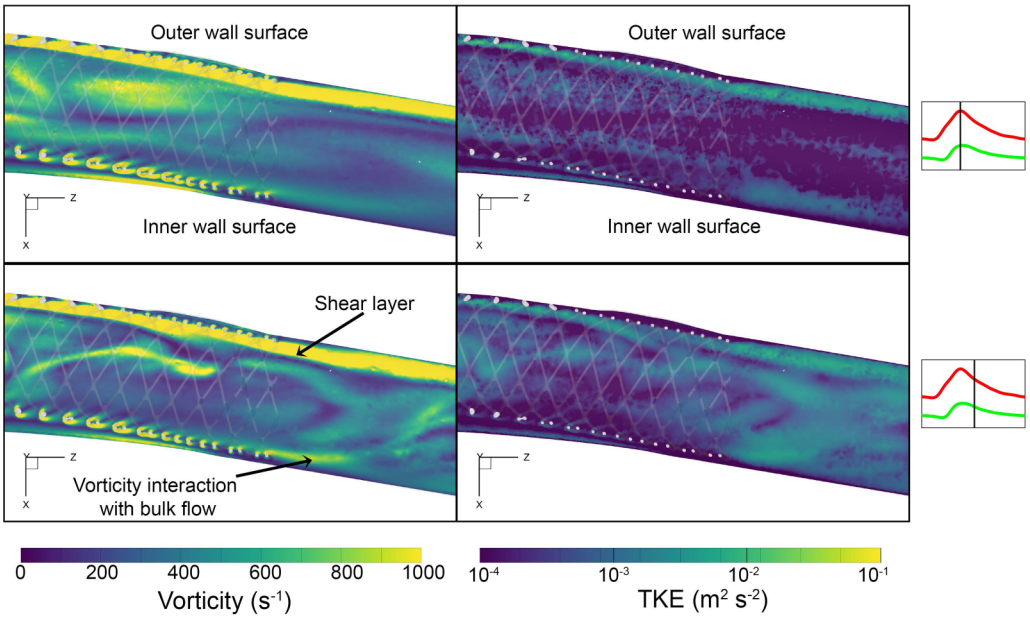

FIG. 7. Contour plots of vorticity magnitude (left) and turbulent kinetic energy (right) on the central plane at the edge of the stent. The distributions have been plotted at the maximum (top) and deceleration (bottom) inlet flow time points for the stented case.

disturbances also tended to grow during the deceleration phase in the tortuous intracranial aneurysm geometries [45].

Although the TKE distribution is much lower in magnitude in the stented AVF, an increase in TKE is noted at the heel of the anastomosis at the maximum time point. The smaller recirculation region in the stented case, noted in Gunasekera *et al.* [21] and Fig. 5, led to lower fluctuations at the heel. The uneven wall surface, created by the stent struts, energized the boundary layer which in turn delays or negates flow separation [46] and its ensuing turbulence generation. The increased TKE noted at the heel of the stented case extended downstream along the stent at the maximum inlet flow time point. However, at the deceleration time point this extended region of TKE starting from the heel of the AVF broke down into isolated smaller regions, again highlighting the increase in disturbances in the deceleration phase. Importantly, these fluctuations were constrained within the stent encapsulated region in the malapposed vein, with the stent acting as a buffer funnelling the turbulent fluctuations away from the vessel wall.

C. Turbulence generation at the downstream edge of the stent implantation

Although the noted TKE is much lower in the stented case, there is an increase in TKE magnitude (relative to other regions in the stented case) after the end of the stent. This increase in disturbance is seen most clearly in the deceleration phase of the inlet flow waveform. A study measuring shear stress of stented *in vitro* vessels noted the presence of disturbances downstream of the stent implantation [47]. The authors postulated that the struts could behave similar to a cylinder placed in a cross-flow where the oscillating vortices shed from the cylinder become unstable with flow over a certain Reynolds number. A recent PIV measurement of a stent-graft in an *in vitro* compliant model noted a recirculation zone at the trailing edge that was postulated to be caused by the compliance mismatch between the graft and the artery [48]. Vorticity magnitude was plotted across a central plane at the stent edge, as illustrated in Fig. 7 to assess the span-wise vortical behavior suggested in other studies. The magnitude (rather than a component) of the vorticity was used to avoid complications that arise with aligning the tortuous vessel with the principal axes.

The vortical behavior is relatively low in the bulk flow of the vessel except at the deceleration phase where there is a high vorticity region coming off the heel of the anastomosis. Dean vortices that are created at the curved anastomosis breakdown in the deceleration phase due to the rotational energy being unsustainable with the decrease in momentum provided by the inlet flows. The magnitude of this feature reduces as the flow approaches the edge of the stent. More complex vortical behavior is initiated in the bulk flow past the proximal edge of the stent (at the deceleration time point). These complex regions are co-located with regions of nonzero TKE as well.

Another striking feature is the high vorticity magnitude region at the stent struts. This behavior is persistent throughout the cycle, however, the interaction between the vortical flow from adjacent stent struts is much higher at the outer wall surface (refer to the first row of Fig. 7 for the inner/outer wall surface localities). The coalescing vortical flow structures amount to a shear layer forming and shielding the stent encapsulated flow. Studies on an idealized coronary artery geometry noted the coalescing of vortical regions with stent struts of shorter gaps as opposed to the creation of individual recirculation zones with longer strut gaps [49]. However, in the current study, the stronger cohesion between adjacent vortical regions in the outer wall surface is due to the relatively higher velocity flow traversing the outer curved AVF anastomosis.

The shear layer is seen to continue past the stent edge at the outer wall surface, however, the shear layer at the inner wall surface is seen to interact with the aforementioned bulk flow complexities. This increase in magnitude and traversal of vortical flow towards the bulk flow region was noted in PIV studies of flow around a spanwise cylinder close to a wall [50], where, at a critical gap width, the vortices created from the gap flow interact with the upper vortices. This vortical flow interaction leads to a significant increase in TKE downstream of the stent edge during the deceleration phase. Figure 7 illustrates the vortical flow interaction and the resulting TKE increase on one plane, however, this behavior is expected throughout the cross-section of the vessel circumscribed by the stent edge.

IV. IMPACT OF THE TURBULENCE GENERATION ON THE WALL SHEAR STRESSES

The patient-specific vessel wall was unwrapped onto a 2D surface to illustrate the effects of the bulk flow features on the wall. The vessel centerline node locations, obtained using the Vascular Modelling Toolkit software (VMTK), together with the vessel wall locations were utilized for this unwrapping procedure. A local centerline node direction vector can be calculated using a central difference of the two adjacent centerline node locations. Another direction vector, perpendicular to the local centerline direction vector, was created such that it pointed to the inner surface of the vessel from the centerline node. In the case of the outlet vein, the inner half of the vessel was the half that was closest to the proximal artery vessel, and viceversa. The inner surface of the distal artery was also determined relative to the location of the proximal artery. Following these two steps provides a local axial vector and an auxiliary in-plane (vessel cross-section) vector to calculate distances away from the anastomosis and angles relative to the inner surface, respectively, at each node. Examples of the axial vector and the auxiliary in-plane vector have been illustrated at selected centerline nodes in Fig. 8.

The next step was to assign each wall element to its closest centerline node. Using the in-plane vector, an angle was measured for each of these assigned wall elements relative to the inner surface of the vessel. Assuming that the vessel cross-sections were close to circular, a circumferential distance of the wall element from the inner surface could be calculated using the aforementioned angle and the distance of the wall element from the centerline node.

Following these steps yields an axial location along the vein and a circumferential location along the cross-section of the vessel for each wall element, thereby converting the prior 3D vessel wall surface to a 2D surface (Fig. 8). The spacing of the centerline nodes was reduced to 0.1 mm increments to decrease unnatural steps in the plot. The clarity obtained by visualizing the whole tortuous vessel on a plane outweighed the effects of the circularity assumption.

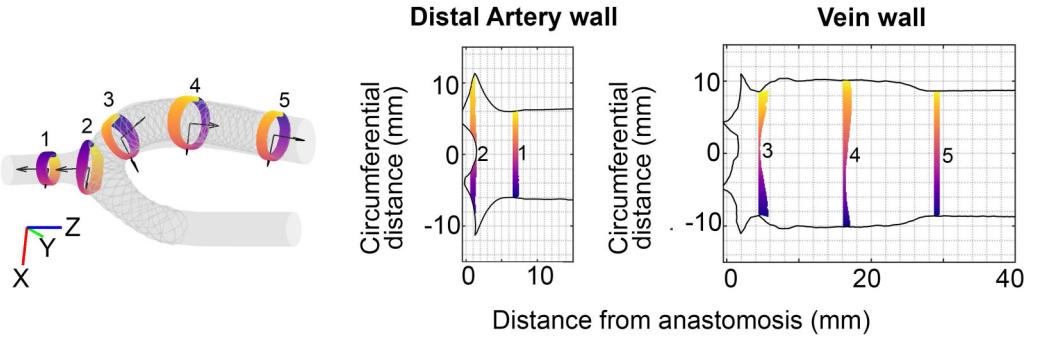

FIG. 8. Example of unwrapping the 3D vessel wall locations onto a 2D space using local vectors constructed from centerline node locations. The color bar of the cross-sectional slices assist with understanding the 3D location of the wall element on the corresponding 2D plots.

To quantify the impact of the bulk flow features on the vessel, both cycle-averaged and phase-averaged WSS metrics have been used. Distributions of TAWSS, defined by Eq. (4), are used to note regions of low TAWSS which is inter-related to regions of near-wall low velocity. The oscillatory shear index (OSI) captures the level of reversal of the WSS vector along the line of the dominant WSS vector [51] and is calculated using Eq. (5). Additionally, the TAWSS metric only provides a mean measure, while the OSI only captures the fluctuation along a single direction. Because of these deficiencies, additional WSS metrics were introduced, one of which is transverse wall shear stress (transWSS). This metric attempts to capture the multidirectional variation of the WSS vector across the cardiac cycle and is calculated by Eq. (6):

$$\mathrm{TAWSS} = \frac{1}{T}\int_0^T |\overrightarrow{\mathrm{WSS}}|\, dt, \tag{4}$$

$$\mathrm{OSI} = 0.5\left(1 - \frac{\frac{1}{T}\left|\int_0^T \overrightarrow{\mathrm{WSS}}\, dt\right|}{\mathrm{TAWSS}}\right), \tag{5}$$

$$\mathrm{transWSS} = \frac{1}{T}\int_0^T \left|\overrightarrow{\mathrm{WSS}} \cdot \left(\vec{n} \times \frac{\int_0^T \overrightarrow{\mathrm{WSS}} dt}{\left|\int_0^T \overrightarrow{\mathrm{WSS}} dt\right|}\right)\right| dt. \tag{6}$$

In a similar fashion to the calculation of phase-averaged TKE, the phase-averaged turbulent fluctuations of WSS were also calculated at the maximum and deceleration time points in the cycle. Using the fluctuations for each component of the WSS vector ($\overrightarrow{\mathrm{WSS}}$), $\mathrm{WSS}'_x = \mathrm{WSS}_x - \overline{\mathrm{WSS}_x}$, $\mathrm{WSS}'_y = \mathrm{WSS}_y - \overline{\mathrm{WSS}_y}$, $\mathrm{WSS}'_z = \mathrm{WSS}_z - \overline{\mathrm{WSS}_z}$, the magnitude of the WSS fluctuations were calculated as follows and shall be referred to as Turbulent Wall Shear Stress (TWSS). TWSS values have been phase-averaged across 12 cycles to capture persistent distributions.

$$\mathrm{TWSS} = \sqrt{\left(\mathrm{WSS}'^2_x + \mathrm{WSS}'^2_y + \mathrm{WSS}'^2_z\right)}. \tag{7}$$

A. Behavior of the WSS at the distal artery

There is a clear low TAWSS region in the distal artery near the anastomosis for both the stented and stent-absent cases. This is to be expected as the collision of the two inlet flows creates a recirculation zone near the floor of the anastomosis. Since the trajectory of the coalesced flow is directed towards the vein and the high velocity flow moves towards the outer wall of the vessel (relating to the maximum circumferential distances in Fig. 9), the TAWSS starts increasing in the anastomosis. The increase is more sudden and persistent in the stent-absent case compared to the

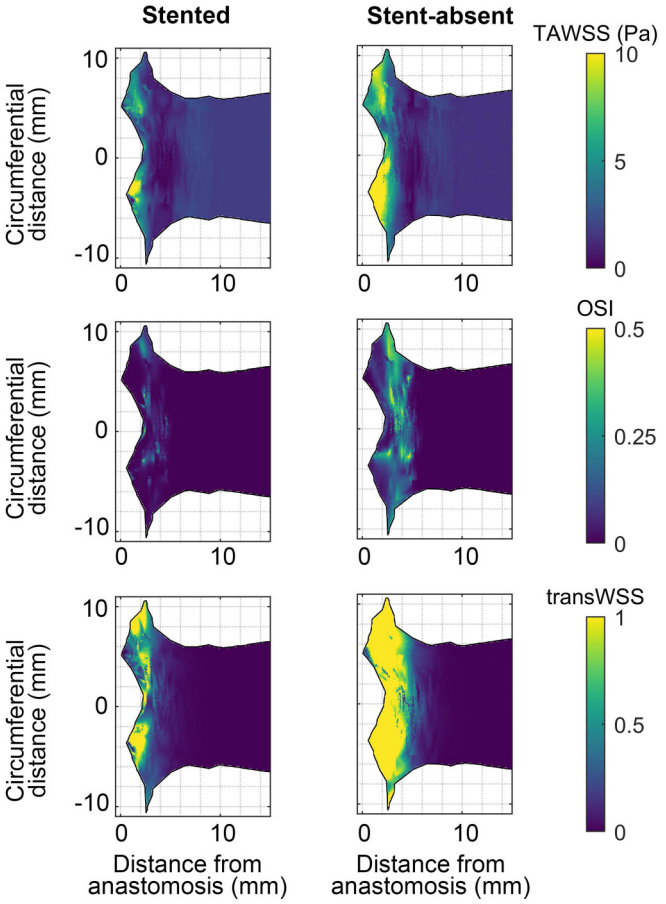

FIG. 9. Wall shear stress metrics on vessel wall at the distal artery.

stented case. This is due to the stent implantation inhibiting the high velocity flow from being incident on large sections of the vessel wall.

In the stent-absent case, large regions of high OSI are noted in the same regions where low TAWSS was observed. Similar patterns are noted in the stented case as well, however, the magnitude and spread of these regions are very much subdued. The generation of high TKE in the anastomosis of the stent-absent model could explain the high regions of oscillating wall shear stresses. However, transWSS is a better metric to assess multidirectional disturbances in the anastomosis. As expected, there are much larger regions of high transWSS noted in the stent-absent case when compared to that of the stented case. An important observation is that the high transWSS and OSI regions of the stent-absent AVF case are adjacent or coincident with the band of low TAWSS.

B. Behavior of the WSS in the juxta-anastomotic vein

The distribution of the cycle-averaged WSS metrics: TAWSS, OSI, and transWSS, across the vein is illustrated in Fig. 10. A clear difference between the stented and stent-absent cases is noted at the heel region of the vein. A large TAWSS accompanied by a large ring of high OSI is noted in the stent-absent case, however, the stent-absent case shows a much smaller region of high OSI. The funnelling capability of the porous stent is a major contributing factor to the decrease in OSI [21]. The disturbances generated in the anastomosis are kept away from the vessel wall in the malapposed

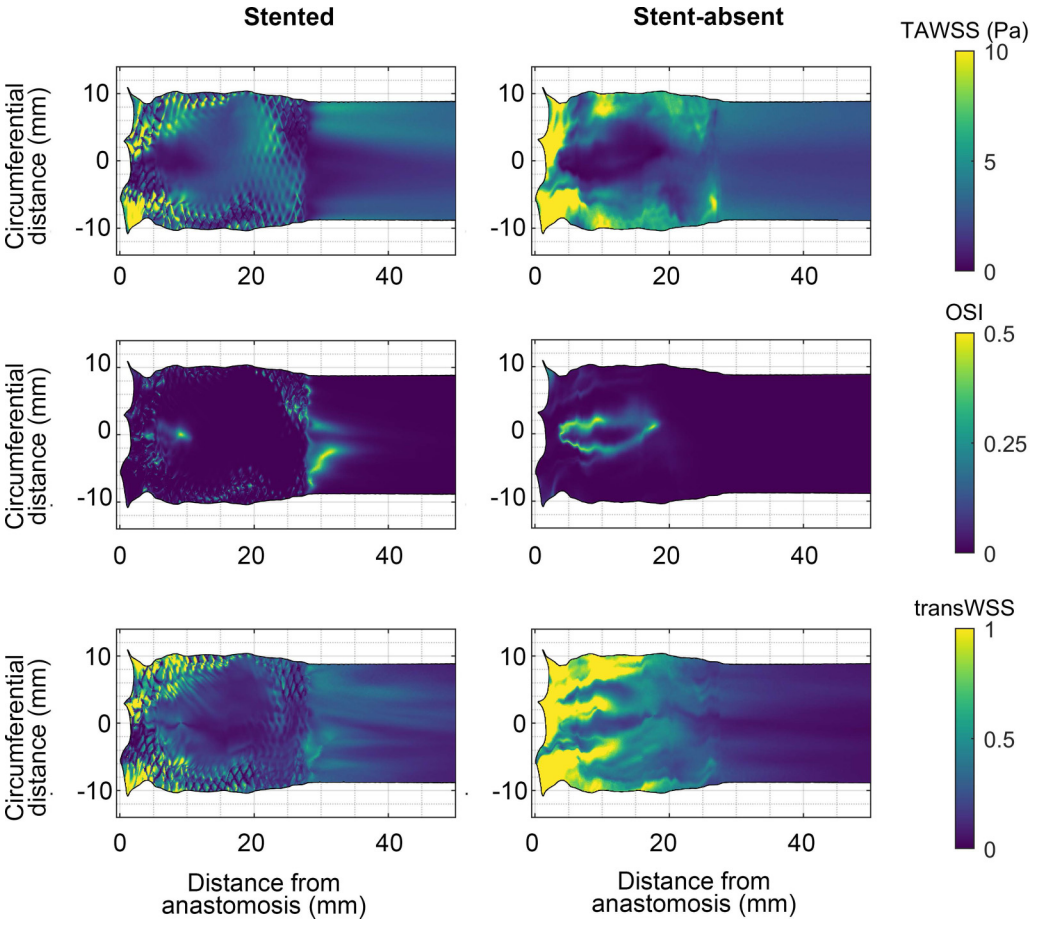

FIG. 10. Wall shear stress metrics on vessel wall at the proximal vein.

region of the vessel. The impact of the shorter recirculation zone results in a shorter region of low TAWSS in the stented case.

There is a large distribution of high transWSS on either side of the recirculation zone in the stent-absent case, with the magnitude decreasing at the downstream edge of the recirculation zone. There is also a large distribution of high transWSS at the outer surface of the vein (relating to the maximum circumferential distances in Figs. 10 and 11). The oscillatory flow behavior that was initiated at the interface and conveyed along the outer bounds of the vein (as detailed with the temporal flow rate ratios of Sec. III A) would lead to the vessel wall continually sensing a high and low velocity gradient across the cycle, with variations in the WSS vector direction. These flow oscillations were very much tempered in the stented case which resulted in a smaller distribution of the high transWSS.

To better understand the impact of the TKE flow behavior, the distribution of the TWSS has been considered at the maximum and deceleration time points in Fig. 11. A persistent high TWSS region is seen at the outer regions of the vessel wall near the anastomosis in the stent-absent case throughout the cycle. A possible contributor to these fluctuations in WSS is the TKE generated at the interface of the two inlets. High amplitude oscillations were noted at the first three monitor points in the vein (refer to Fig. 4) and the variation in the velocity magnitude distribution is significant at the outer wall of the vein (refer to Fig. 5). The TWSS affirms that the cycle-to-cycle variations in

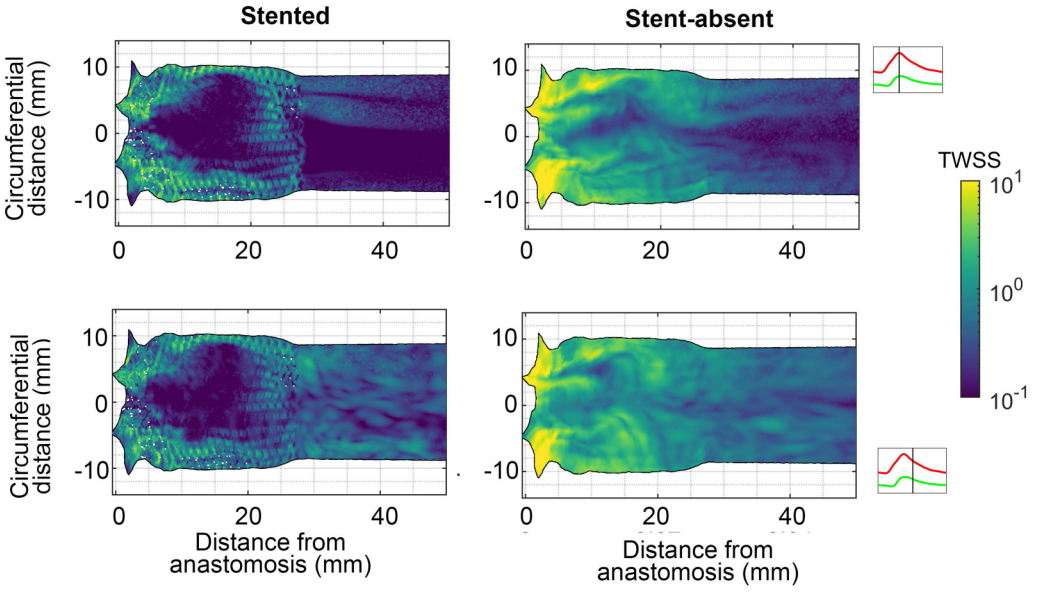

FIG. 11. Turbulent wall shear stress distribution at the maximum (top) and deceleration (bottom) time points across the proximal vein.

the oscillatory flow also translate to cycle-to-cycle variations in the WSS. The TWSS is an order of magnitude lower near the heel of the anastomosis. Low TWSS is surrounded by a region of relatively higher TWSS, in a manner similar to that of the TAWSS and transWSS distributions. This behavior is more apparent at the maximum time point. The low velocity flow present at the heel would yield relatively lower magnitude fluctuations leading to lower fluctuations in the WSS as well. However, the variation of the extent of the recirculation zone leads to the high WSS fluctuations bordering the low velocity region.

The main behavior seen in the stented case is that the high TWSS is concentrated to the stent strut regions. Studies have shown the presence of recirculation zones in the spaces between struts of apposed [52] and malapposed [16] stent segments. The disturbances caused in these microrecirculation zones coupled with the high velocity flow traversing on the outer edge of the vessel yield significantly high levels of TWSS localized to the stent strut spaces. It is also clear that these dynamics localized around strut regions and effects of fluctuating bulk flow are not propagated to the vessel in the malapposed region where the TWSS magnitude is significantly low.

C. WSS behavior proximal to the stent implantation

The WSS behavior appears to be generally homogeneous in the stented case downstream of the heel until the flow reaches the stent edge. There is an increase of OSI and transWSS at the inner vessel wall (relating to a circumferential distance of zero in Fig. 10). The increase in these WSS measures is co-located with a decrease in TAWSS which would be caused by the recirculating flow emanating from the malapposed stent edge. The decrease in shear stress and presence of recirculatory flow has also been noted in simulations of peripheral arteries with insufficient stent-graft apposition [53]. The variation of the vortical flow emanating from the stent edge leads to the increase in the transWSS and OSI which spans an extent of approximately 7.5 mm downstream of the stent-edge.

The TWSS magnitude is low downstream of the stent-edge at the maximum time point. However, there is a streak of high TWSS on the outer vessel wall caused by the higher velocity flow and the shear layer extending off the outer circumference of the stent-edge. This streak of high TWSS

continually decreases in magnitude downstream of the vessel. The magnitude of this high TWSS feature is still approximately an order of magnitude lower than the regions surrounding the struts that are located on the outer walls and near the anastomosis.

The TWSS distribution at the deceleration time point is very different, with the whole vessel wall covered by clumps of relatively high TWSS regions. The dynamics of the interactions of the multiple vortices (detailed in Sec. III C) lead to a sudden increase in the TKE near the wall that subsequently affects the near-wall velocity gradients as well. The increased fluctuating near-wall dynamics caused by the stent edge could lay claim to the build-up of IH downstream of stent implantations noted in aorta subjects [54] and could potentially affect stented AVFs in a similar manner.

V. CONCLUSION

Large eddy simulations of the flow within a single patient-specific AVF, with and without a stent implantation, were conducted. Oscillatory behavior was noted to be originating from the distal toe of the anastomosis of the AVF. The frequency peaks of the oscillatory behavior were much larger in the stent-absent case. This behavior was noted to continue throughout the inlet cardiac cycle, however, the subdued oscillatory flow in the stented case persisted in the deceleration phase of the inlet flow. Furthermore, a high TKE region was consistently noted at the interface of the two inlet flows at all analyzed time points in the stent-absent case. This coincidence in findings confirms that the oscillatory flow behavior is involved in the generation of turbulent flow in the anastomosis which is conveyed towards the vein. The levels of TKE in the anastomosis of the stented case were far lower indicating that the presence of the stent at the location of the inlet flow interface could mitigate the flow disturbances.

An increase in TKE levels was also noted at the heel of the stent-absent AVF anastomosis at the maximum and deceleration time points. These flow features led to a ring of high WSS fluctuations within the cycle (OSI, transWSS) and across cycles (TWSS). The increase in TKE was far less significant in the stented case and these disturbances were held within the stent encapsulated region. The stent circumvented these minor disturbances away from the vessel walls thereby resulting in a smaller region of adverse WSS behavior at the heel of the AVF. However, there were localized regions of high WSS fluctuations surrounding the stent struts due to the generation of microrecirculation regions.

Although the fluctuating hemodynamics of the stented case were far less apparent than that of the stent-absent case, an increase in TKE was noted at the downstream edge of the stent which was malapposed from the inner vessel wall. Complex vortical flow behavior emanating from this malapposed stent edge acted as a catalyst in the increase in flow disturbances, particularly at the deceleration time point of the inlet flow. These observations were mirrored with the TWSS measurements which also increased downstream of the stent edge.

Therefore, the stent placement mitigated the initiation of TKE and the malapposition at the heel shielded the vessel from the low levels of turbulent flow conveyed downstream from the anastomosis. However, the malapposition at the stent edge could potentially create adverse disease-causing flow conditions downstream of the implantation. This detailed investigation of the vascular procedure provides key understanding of the reasons behind the success of this treatment strategy (in this patient case) from a fluid dynamics perspective.

ACKNOWLEDGMENTS

Sanjiv Gunasekera and Olivia Ng were recipients of the Australian Government Research Training Program Scholarship during the course of this work and gratefully acknowledge this support.

APPENDIX: TURBULENT KINETIC ENERGY CALCULATIONS

The resolved turbulent kinetic energy was calculated using a phase-averaged approach to account for the pulsatile nature of the flow domain. Phase-averaged turbulent kinetic energy was calculated

using Eq. (A1) at specific time points in the cardiac cycle:

$$\mathrm{TKE}_{\mathrm{resolved}} = \tfrac{1}{2}\left(u'^2_x + u'^2_y + u'^2_z\right). \tag{A1}$$

Here, $u'_x = U_x - \overline{U_x}$, $u'_y = U_y - \overline{U_y}$, and $u'_z = U_z - \overline{U_z}$ correspond to the instantaneous velocity fluctuations, where $\overline{U_x}$, $\overline{U_y}$, and $\overline{U_z}$ are the phase-averaged velocities. In addition to the maximum and minimum time points, $\mathrm{TKE}_{\mathrm{resolved}}$ was calculated at two points in the acceleration phase and three points in the deceleration phase. This approach was necessary as calculating $\mathrm{TKE}_{\mathrm{resolved}}$ for all time points would have overwhelmed the storage resources due to the small time-step and grid size. The $\mathrm{TKE}_{\mathrm{resolved}}$ was phase-averaged over 12 cycles to ensure that the quantity was converged. A user-defined function was employed to update the phase-averaged quantities on each passing cycle in an efficient manner. The unresolved turbulent kinetic energy (contained within the subgrid) was estimated using the following equations:

$$\mathrm{TKE}_{\mathrm{unresolved}} = \frac{(C_S \Delta S)^2}{0.3}, \tag{A2}$$

$$\Delta = [6\sqrt{2}(\text{cell-volume})]^{1/3}, \tag{A3}$$

$$\text{proportion of } \mathrm{TKE}_{\mathrm{resolved}} = \frac{\mathrm{TKE}_{\mathrm{resolved}}}{\mathrm{TKE}_{\mathrm{resolved}} + \mathrm{TKE}_{\mathrm{unresolved}}}, \tag{A4}$$

where Δ is the subgrid length of the tetrahedral elements and S is the strain rate magnitude as calculated within the solver [55].

[1] D. Santoro, F. Benedetto, P. Mondello, N. Pipitò, D. Barillà, F. Spinelli, C. A. Ricciardi, V. Cernaro, and M. Buemi, Vascular access for hemodialysis: Current perspectives, Int. J. Nephrol. Renovasc. Dis. **7**, 281 (2014).

[2] J. C. Duque, M. Tabbara, L. Martinez, J. Cardona, R. I. Vazquez-Padron, and L. H. Salman, Dialysis arteriovenous fistula failure and angioplasty: Intimal hyperplasia and other causes of access failure, Amer. J. Kidney Dis. **69**, 147 (2017).

[3] D. Fulker, B. Ene-Iordache, and T. Barber, High-resolution computational fluid dynamic simulation of haemodialysis cannulation in a patient-specific arteriovenous fistula, J. Biomech. Eng. **140**, 031011 (2018).

[4] M. Bozzetto, B. Ene-Iordache, and A. Remuzzi, Transitional flow in the venous side of patient-specific arteriovenous fistulae for hemodialysis, Ann. Biomed. Eng. **44**, 2388 (2016).

[5] S. Stella, C. Vergara, L. Giovannacci, A. Quarteroni, and G. Prouse, Assessing the disturbed flow and the transition to turbulence in the arteriovenous fistula, J. Biomech. Eng. **141**, 101010 (2019).

[6] S. Gunasekera, O. Ng, S. Thomas, R. Varcoe, C. de Silva, and T. Barber, Tomographic PIV analysis of physiological flow conditions in a patient-specific arteriovenous fistula, Exp. Fluids **61**, 1 (2020).

[7] S. S. Varghese, S. H. Frankel, and P. F. Fischer, Direct numerical simulation of stenotic flows. Part 2. Pulsatile flow, J. Fluid Mech. **582**, 281 (2007).

[8] A. Remuzzi and B. Ene-Iordache, Novel paradigms for dialysis vascular access: Upstream hemodynamics and vascular remodeling in dialysis access stenosis, Clin. J. Amer. Soc. Nephrol. **8**, 2186 (2013).

[9] M. Mallik, R. Sivaprakasam, G. J. Pettigrew, and C. J. Callaghan, Operative salvage of radiocephalic arteriovenous fistulas by formation of a proximal neoanastomosis, J. Vasc. Surg. **54**, 168 (2011).

[10] S. Anwar and T. J. Vachharajani, Stent use for hemodialysis access: What a general nephrologist needs to know, Hemodial. Intl. **22**, 143 (2017).

[11] D. Stoeckel, A. Pelton, and T. Duerig, Self-expanding nitinol stents: Material and design considerations, Eur. Radiol. **14**, 292 (2004).

[12] J. Swinnen, K. L. Tan, R. Allen, D. Burgess, and I. V. Mohan, Juxta-anastomotic stenting with aggressive angioplasty will salvage the native radiocephalic fistula for dialysis, J. Vasc. Surg. **61**, 436 (2015).

[13] S. D. Thomas, S. Peden, P. Crowe, and R. L. Varcoe, Interwoven nitinol stents to treat radiocephalic anastomotic arteriovenous fistula stenosis, J. Endovasc. Ther. **26**, 394 (2019).

[14] S. D. Thomas, S. Peden, N. Katib, P. Crowe, T. Barber, and R. L. Varcoe, Long-term results of interwoven nitinol stents to treat the radiocephalic anastomotic arteriovenous fistula stenosis, J. Endovasc. Ther. (2022), doi:10.1177/15266028221075230.

[15] J. W. Van Werkum, A. A. Heestermans, A. C. Zomer, J. C. Kelder, M.-J. Suttorp, B. J. Rensing, J. J. Koolen, B. G. Brueren, J.-H. E. Dambrink, R. W. Hautvast *et al.*, Predictors of coronary stent thrombosis: The dutch stent thrombosis registry, J. Am. Coll. Cardiol. **53**, 1399 (2009).

[16] W. X. Chen, E. K. Poon, V. Thondapu, N. Hutchins, P. Barlis, and A. Ooi, Haemodynamic effects of incomplete stent apposition in curved coronary arteries, J. Biomech. **63**, 164 (2017).

[17] S. Beier, J. Ormiston, M. Webster, J. Cater, S. Norris, P. Medrano-Gracia, A. Young, and B. Cowan, Hemodynamics in idealized stented coronary arteries: Important stent design considerations, Ann. Biomed. Eng. **44**, 315 (2016).

[18] H. Y. Chen, J. Hermiller, A. K. Sinha, M. Sturek, L. Zhu, and G. S. Kassab, Effects of stent sizing on endothelial and vessel wall stress: Potential mechanisms for in-stent restenosis, J. Appl. Physiol. **106**, 1686 (2009).

[19] L. Wei, J. Wang, Q. Chen, and Z. Li, Impact of stent malapposition on intracoronary flow dynamics: An optical coherence tomography-based patient-specific study, Med. Eng. Phys. **94**, 26 (2021).

[20] E. P.-Y. Huang, M.-F. Li, C.-C. Hsiao, H.-Y. Chen, P.-A. Wu, and H.-L. Liang, Undersized stent graft for treatment of cephalic arch stenosis in arteriovenous hemodialysis access, Sci. Rep. **10**, 1 (2020).

[21] S. Gunasekera, O. Ng, S. Thomas, R. Varcoe, C. de Silva, and T. Barber, Impact of juxta-anastomotic stent implantation on the haemodynamics within a single representative patient AVF, Int. J. Heat Fluid Flow **92**, 108874 (2021).

[22] W. Brinjikji, M. H. Murad, G. Lanzino, H. J. Cloft, and D. F. Kallmes, Endovascular treatment of intracranial aneurysms with flow diverters: A meta-analysis, Stroke **44**, 442 (2013).

[23] E. Colley, J. Carroll, S. Thomas, R. L. Varcoe, A. Simmons, and T. Barber, A methodology for noninvasive 3D surveillance of arteriovenous fistulae using freehand ultrasound, IEEE Trans. Biomed. Eng. **65**, 1885 (2018).

[24] S. Gunasekera, O. Ng, S. Thomas, R. Varcoe, C. de Silva, T. Barber *et al.*, A numerical investigation of a stented arteriovenous fistula, in *Proceedings of the 22nd Australasian Fluid Mechanics Conference*, edited by H. Chanson and R. Brown (University of Queensland Press, Brisbane, 2020)

[25] J. E. Carroll, E. S. Colley, S. D. Thomas, R. L. Varcoe, A. Simmons, and T. J. Barber, Tracking geometric and hemodynamic alterations of an arteriovenous fistula through patient-specific modelling, Comput. Methods Prog. Biomed. **186**, 105203 (2020).

[26] K. Valen-Sendstad, K.-A. Mardal, M. Mortensen, B. A. P. Reif, and H. P. Langtangen, Direct numerical simulation of transitional flow in a patient-specific intracranial aneurysm, J. Biomech. **44**, 2826 (2011).

[27] M. Germano, U. Piomelli, P. Moin, and W. H. Cabot, A dynamic subgrid-scale eddy viscosity model, Phys. Fluids **3**, 1760 (1991).

[28] D. K. Lilly, A proposed modification of the Germano subgrid-scale closure method, Phys. Fluids **4**, 633 (1992).

[29] F. Nicoud and F. Ducros, Subgrid-scale stress modelling based on the square of the velocity gradient tensor, Flow, Turbul. Combust. **62**, 183 (1999).

[30] F. Nicoud, H. B. Toda, O. Cabrit, S. Bose, and J. Lee, Using singular values to build a subgrid-scale model for large eddy simulations, Phys. Fluids **23**, 085106 (2011).

[31] E. Jabir and S. A. Lal, Numerical analysis of blood flow through an elliptic stenosis using large eddy simulation, Proc. Inst. Mech. Eng., Part H: J. Eng. Med. **230**, 709 (2016).

[32] A. Pal, K. Anupindi, Y. Delorme, N. Ghaisas, D. A. Shetty, and S. H. Frankel, Large eddy simulation of transitional flow in an idealized stenotic blood vessel: Evaluation of subgrid scale models, J. Biomech. Eng. **136**, 071009 (2014).

[33] F. P. P. Tan, N. B. Wood, G. Tabor, and X. Y. Xu, Comparison of LES of steady transitional flow in an idealized stenosed axisymmetric artery model with a RANS transitional model, J. Biomech. Eng. **133**, 051001 (2011).

[34] V. Mancini, A. W. Bergersen, J. Vierendeels, P. Segers, and K. Valen-Sendstad, High-frequency fluctuations in post-stenotic patient specific carotid stenosis fluid dynamics: A computational fluid dynamics strategy study, Cardiovasc. Eng. Technol. **10**, 277 (2019).
[35] O. Ng, S. D. Gunasekera, S. D. Thomas, R. L. Varcoe, and T. J. Barber, The effect of assumed boundary conditions on the accuracy of patient-specific cfd arteriovenous fistula model, Comput. Methods Biomech. Biomed. Eng.: Imag. Visual. 1 (2022).
[36] I. B. Celik, U. Ghia, P. J. Roache *et al.*, Procedure for estimation and reporting of uncertainty due to discretization in CFD applications, J. Fluids Eng. **130**, 078001 (2008).
[37] S. B. Pope, Turbulent flows, Meas. Sci. Technol. **12**, 2020 (2001).
[38] R. Courant, K. Friedrichs, and H. Lewy, On the partial difference equations of mathematical physics, IBM J. Res. Dev. **11**, 215 (1967).
[39] P. M. McGah, D. F. Leotta, K. W. Beach, and A. Aliseda, Effects of wall distensibility in hemodynamic simulations of an arteriovenous fistula, Biomech. Model. Mechanobiol. **13**, 679 (2014).
[40] P. R. Vijayaratnam, C. C. O'Brien, J. A. Reizes, T. J. Barber, and E. R. Edelman, The impact of blood rheology on drug transport in stented arteries: Steady simulations, PLoS One **10**, e0128178 (2015).
[41] Y. I. Cho and K. R. Kensey, Effects of the non-Newtonian viscosity of blood on flows in a diseased arterial vessel. Part 1: Steady flows, Biorheology **28**, 241 (1991).
[42] See Supplemental Material at http://link.aps.org/supplemental/10.1103/PhysRevFluids.7.123101 for the instantaneous velocity magnitude across the central plane in both the stented and stent-absent AVF geometries.
[43] T. Lu, P. Jiang, Z. Guo, Y. Zhang, and H. Li, Large-eddy simulations (LES) of temperature fluctuations in a mixing tee with/without a porous medium, Int. J. Heat Mass Transf. **53**, 4458 (2010).
[44] L. D. Browne, M. T. Walsh, and P. Griffin, Experimental and numerical analysis of the bulk flow parameters within an arteriovenous fistula, Cardiovasc. Eng. Technol. **6**, 450 (2015).
[45] K. Valen-Sendstad, M. Piccinelli, and D. A. Steinman, High-resolution computational fluid dynamics detects flow instabilities in the carotid siphon: Implications for aneurysm initiation and rupture, J. Biomech. **47**, 3210 (2014).
[46] J. Lin, F. Howard, D. Bushnell, and G. Selby, Investigation of several passive and active methods for turbulent flow separation control, in *Proceedings of the 21st Fluid Dynamics, Plasma Dynamics, and Lasers Conference, Seattle, WA* (AIAA, Reston, VA, 1990), p. 1598.
[47] J. Peacock, S. Hankins, T. Jones, and R. Lutz, Flow instabilities induced by coronary artery stents: assessment with an *in vitro* pulse duplicator, J. Biomech. **28**, 17 (1995).
[48] S. G. Yazdi, P. D. Docherty, A. Khanafer, M. Jermy, N. Kabaliuk, P. H. Geoghegan, and P. Williamson, *In vitro* particle image velocimetry assessment of the endovascular haemodynamic features distal of stent-grafts that are associated with development of limb occlusion, J. Roy. Soc. New Zealand **51**, 361 (2021).
[49] J. L. Berry, A. Santamarina, J. E. Moore, S. Roychowdhury, and W. D. Routh, Experimental and computational flow evaluation of coronary stents, Ann. Biomed. Eng. **28**, 386 (2000).
[50] G.-S. He, J.-J. Wang, C. Pan, L.-H. Feng, Q. Gao, and A. Rinoshika, Vortex dynamics for flow over a circular cylinder in proximity to a wall, J. Fluid Mech. **812**, 698 (2017).
[51] X. He and D. N. Ku, Pulsatile flow in the human left coronary artery bifurcation: Average conditions, J. Biomech. Eng. **118**, 74 (1996).
[52] J. M. Jiménez and P. F. Davies, Hemodynamically driven stent strut design, Ann. Biomed. Eng. **37**, 1483 (2009).
[53] R. Al-Hakim, E. Lee, S. Kee, K. Seals, B. Varghese, A. Chien, M. Quirk, and J. McWilliams, Hemodynamic analysis of edge stenosis in peripheral artery stent grafts, Diagn. Intervent. Imag. **98**, 729 (2017).
[54] K. H. Barth, R. Virmani, E. P. Strecker, M. A. Savin, D. Lindisch, A. H. Matsumoto, and G. P. Teitelbaum, Flexible tantalum stents implanted in aortas and iliac arteries: Effects in normal canines, Radiology **175**, 91 (1990).
[55] J. Schütze, Y. Egorov, R. Lechner, M. Gritskevich, A. Garbaruk, and A. Gerasimov, Best Practice: Scale-Resolving Simulations in Ansys CFD, ANSYS Germany GmbH, Darmstadt (2015), https://www.ansys.com/content/dam/product/fluids/cfd/tb-best-practices-scale-resolving-models.pdf.